Digital Holography for particle characterization: hologram modeling, refractive index measurement, and optical compression

F. R.A. Onofri, Lilian Chabrol, Fabrice Lamadie, Matthias Sentis, Paul Bresson

The 14th International Conference on
Laser-light and Interactions with Particles (LIP2024)
September 18-22nd, 2024, Xi'an, Shaanxi, China

DIGITAL HOLOGRAPHY FOR PARTICLE CHARACTERIZATION: HOLOGRAM MODELING, REFRACTIVE INDEX MEASUREMENT, AND OPTICAL COMPRESSION

Fabrice ONOFRI [1*], Lilian CHABROL[1], Paul BRESSON[2], Fabrice LAMADIE[2]

[1] Laboratoire IUSTI - UMR n°7343 CNRS/Aix-Marseille Université, Marseille, 13453, France
[2]CEA, DES, ISEC, DMRC, Univ Montpellier, 30207 Bagnols-sur-Ceze, Marcoule, France

Corresponding author: fabrice.onofri@univ-amu.fr

Abstract

Digital In-Line Holography is a highly attractive optical method for the simultaneous determination of the three-dimensional positions and velocities, the shape and size of particles (drops, bubbles, bacteria, etc.) dispersed in a fluid. In this keynote, after a summary of the basics of the DIH, the authors review their latest contributions to further enhance its capabilities, and most notably on the asymptotic modelling and understanding of hologram formation, refractive index measurements and reduction of the sensor filling rate.

1 Introduction

Digital in-Line Holography (DIH) is an optical technique with unique features for the three-dimensional characterization of particulate media. By recording and analysing a simple greyscale image, it provides simultaneously an estimate of the 3D positions, velocities, shapes (2D), sizes and, as has recently been demonstrated, the refractive index of particles in free space [1, 2] as well as media with a degree of astigmatism [3]. In addition, DIH can be operated either as a direct method (e.g. [3-13]), with backpropagation and blob analysis methods, or as an inverse method, parametric or not (e.g. [14-16]).

Counter-intuitively, the precise holographic characterization of spherical (but also cylindrical and ellipsoidal) particles is made tricky by their high symmetry. The latter induces morphologically dependent resonances, grazing, surface and tunnelling effects that are not considered by actual hologram formation models based on the scalar diffraction theory. Naturally, the latter, which do not take particle refractive index into account, is also inappropriate to infer this particle property.

The Lorenz-Mie theory (LMT) [17] and the Debye series expansion [18] are the reference when considering the electromagnetic scattering of light by spherical particles. However, both require large computational resources or data storage capacities, which are not always compatible with the development of fast and accurate inverse analyses. This is especially true for particles with large size parameters and changing optical properties. This explains the renewed interest in the development of asymptotic models, whether for the analysis of far-field scattering or diffraction patterns [19-27], holograms [6, 28-32], interferometric images [19-21], critical [24, 33-35] or rainbow patterns [36-40].

In this keynote, after summarising the basics of the DIH technique, the authors review their recent contributions to the improvement of this optical particle characterisation technique in terms of modelling and understanding of hologram formation, refractive index measurement and reduction of sensor filling rate.

2 Basics on DIH

2.1 Formation and recording of holograms

DIH records images of the so-called diffraction patterns of the particles be characterised at finite distances [5, 12, 13, 41]. In most situations, the cloud of particles is illuminated by a collimated and coherent beam. The detection system is reduced to an intensity-based image sensor (usually without optics) at a medium distance L from the particles. A commonly accepted approximation is that, for a single particle, the recorded pattern results from the interference of the wave it scatters (probe wave, field E_s and intensity I_s), with the wave incident on the sensor (reference wave, field E_r and intensity I_r), see Figure 1 a. For a dilute particle medium, the incident wave is little disturbed as it passes through, $E_r \approx E_0$ and $I_r \approx I_0 = E_0 E_0^*$, and the intensity of the scattered field is negligible compared to that of the incident wave, $I_s / I_0 \approx 0$. Measuring the intensity without particles I_0, we have on the sensor:

$$I/I_0 - 1 \propto \Re e\left\{\mathrm{E}_0 \bar{\mathrm{E}}_s + \bar{\mathrm{E}}_0 \mathrm{E}_s\right\} / I_0 \qquad (1)$$

The term in brackets is a classic two-wave interference term. However, it is referred to as a "hologram" because it results mainly from the interference of diffractive contributions with the reference wave. When k particles are scattered in the probe zone, the global hologram is simply assumed to be the result of the coherent sum of all contributions.

Two approaches are used to extract from this pattern the three-dimensional position x_k, y_k, z_k and radius a_k of these particles.

2.2 Restitution by backpropagation and image analysis

The global hologram is backpropagated over all distances $z < L$ where particles are likely to be present (i.e. the probed zone). Each image obtained (square of the

reconstructed field) is analysed to determine the presence of a particle in that plane and whether its reconstructed image is in focus. This is determined using focusing indicators based, for example, on the divergence of the phase of the reconstructed field or the contrast of the intensity profile [3, 7, 9, 32, 42]. For this reason, DIH is often referred to as "digital refocusing" and "lensless imaging". Once a particle has been localised in z_k, classical image processing tools (Hough transform, convolutional methods...) are used to determine its centroid, x_k, y_k, and shape (blob analysis).

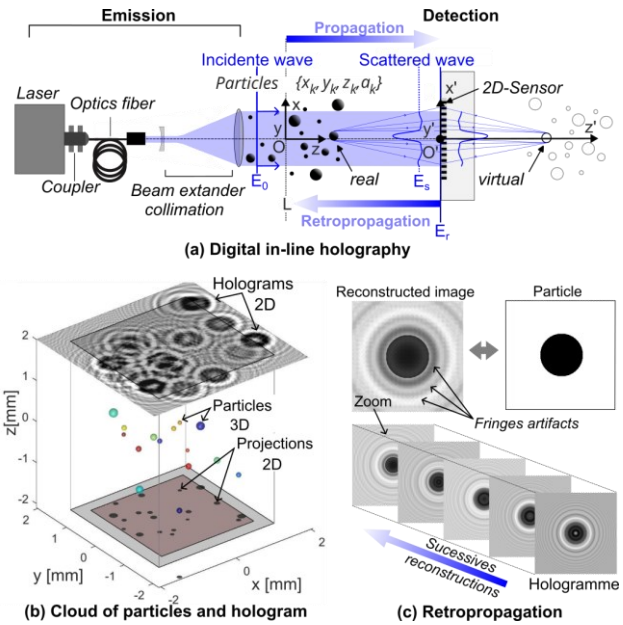

Figure 1 DIH: (a) classical recording setup and illustration of the twin images problem; (b) Global hologram simulated with LMT for n_p=20 particles, with sizes between 80 and 170µm, at a mean distance (on to scale in this graph) of z_c=0.1m for the sensor. (c) Illustration of the principle of the backpropagation approach.

This approach is not restricted to spherical particles. In all cases, the reconstructed images are pixelated and particles with dimensions close to those of the pixels cannot be characterised with this approach. The latter is also very sensitive to the thresholds used to eliminate background noise and detect the particles. Similarly, the images obtained are surrounded by spurious fringes due to the finite size of the sensor and the loss of phase of the recorded interference field, Figure 1 (c). In fact, the bracketed term in Eq. (1) contains two opposing terms. It is as if one term corresponds to the probed particles and the other to virtual particles located symmetrically behind the camera sensor [43]. During the reconstruction process of a particle located at z_k, its image is superimposed by the diffraction pattern of its corresponding virtual particle (also called "twin particle") located at $z = 2L - z_k$..

These fringe artefacts are annoying [44, 45], but not necessarily redhibitory for many applications.

2.3 Restitution by inverse methods

Particles are characterised iteratively by minimising the differences between experimental holograms and those simulated with a scalar diffraction approximation [46-49]. To converge to a global physical solution, this algebraic minimisation requires regularisation based on all available data and a priori (prior measurement of image noise, particle shape, expected bounds on particle size and spatial distribution, etc.). Inverse approaches are no longer limited by the size of the pixels in the particle plane, but rather by the accuracy of the scattering model, the convergence capabilities and the stability of the minimisation method. Particles in the wavelength range can be characterised using the LMT and an optical microscope [7, 46, 50-54]. Particles whose centroid lies outside the surface defined by the matrix sensor can also be characterised to some extent. In this approach, the phase and noise generated by the twin images can even be subtracted computationally [30, 44, 45, 55]. Unfortunately, inverse approaches are extremely expensive in term of computational resources and probably more limited in terms of the density of the particulate medium.

2.4 Basic setup

The simplest setup consists of an unpolarized laser (He-Ne type) of a few milliwatts to tens of milliwatts whose coherence length exceeds the dimensions of the particles. The beam is to clear-up its profile (i.e. monomode fibre, optical pinhole), magnified and collimated. Enlarging the beam attenuates the illumination gradients due to its Gaussian profile, while collimation produces a quasi-planar wavefront at the measurement zone. The high-resolution, high-dynamic CCD or CMOS camera is equipped with the largest possible sensor (1 Mpixel and 12 bits are a minimum). In fact, with no optics in front of the camera, it is the dimensions of the sensor and the width of the beam that determine the lateral dimensions of the observed field. Prior the actual measurements, the intensity I_0 of the particle-free reference wave and I_b that of the electronic noise are measured. The normalised holograms are then given by $(I - I_b)/(I_0 - I_b)$.

3 Holograms simulations with LMT

3.1 Basics

The three components (r,θ,ϕ) of the incident electrical field $E_r^{inc}, E_\theta^{inc}, E_\phi^{inc}$, from a linear or non-polarized incident plane wave, as well as the internal $E_r^{int}, E_\theta^{int}, E_\phi^{int}$ and scattered $E_r^{sca}, E_\theta^{sca}, E_\phi^{sca}$ electrical fields are calculated with series of Legendre's polynomials, Bessel and Hankel functions [17, 56, 57]. Classically, these series are truncated for expansion parameters such as $n \geq n_{stop}$ [58], with $n_{stop} = INT(\alpha_{stop}) + 1$ where $\alpha = \pi D/\lambda$ stands for the particle

size parameter in the considered medium (refractive index m_{ext}) and for the incident wavelength in the embedding medium $\lambda = \lambda_0 / m_{ext}$ with, for instance, $\alpha_{stop} = \alpha + 4.05\alpha^{1/3} + 2$, for $\alpha \in]8, 4200]$.

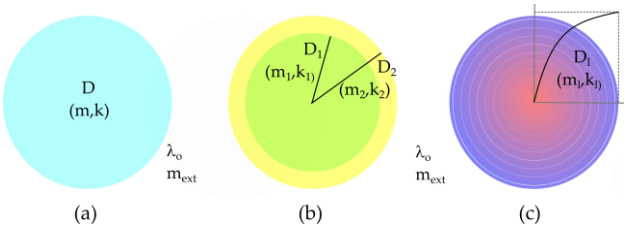

Figure 2 Parameters of spherically symmetric particles [57]

3.2 Speeding up calculations under Matlab's environement

The present authors have developed and made available a set of routines and a MATLAB® application (with a Graphical Unit Interface, GUI), to compute holograms with the LMT in an efficient and convenient way, see Figure 3. The first window allows to manage the calculations, select the interpolation resolution, the output type (scattered or total field), etc. The second allows generation (or import) of different types of particle size distributions, as well as the particle spatial distribution. The third allows the selection the particle material properties, while the fourth collects other setup parameters: sensor distance, pixel size and number, wavelength...

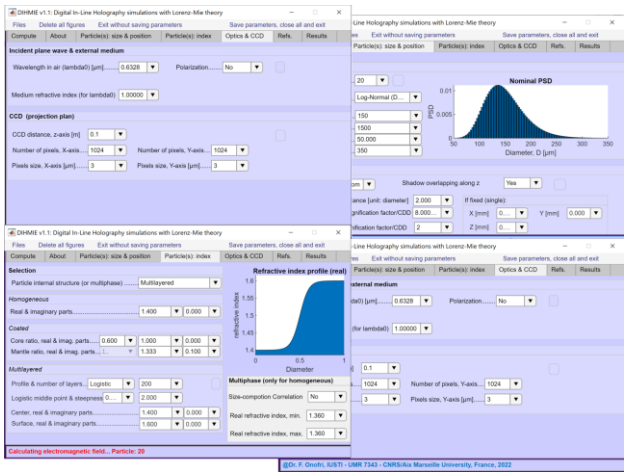

Figure 3 Main windows of the GUI 'DIHMie 1.1'

The particle properties are their 3D coordinates $(x, y, z)_p$ with respect to a laboratory coordinate system $(Oxyz)$, a single complex refractive index (m,k) and diameter D for homogeneous spheres, two complex refractive indices $(m_1, k_1; m_2, k_2)$ and two diameters (D_1, D_2) for coated spheres and a single diameter with up to typically $L = 5000$ complex refractive indices $(m_\ell, k_\ell; \ell = 1, 2, \cdots L)$ for radially inhomogeneous spheres, see Figure 2.

Calculations can be sequential or parallel. Basically, the main output is the intensity of the electromagnetic field on a plane $(x, y, z)_c$ mimicking the surface of the sensor that is perpendicular to the *z-axis* and at located at a distance z_c. The intensity-based sensor, linear, is defined by its pixel size and number. The electromagnetic field considered can be either the incident (reference wave) or, more interestingly, the scattered or the total (scattered plus incident) field of a single particle or a cloud of n_p particles $(D, m, k, x, y, z)_p$. For a cloud of particles, the routines allow accounting for the interference between the fields scattered by all the particles to be considered as if they were alone. In other words, the perturbation of the incident wave by each particle is not neglected, an optical dilute regime is assumed. Other interesting outputs are, for example, the near-field intensity and phase maps or profiles, see Figure 4.

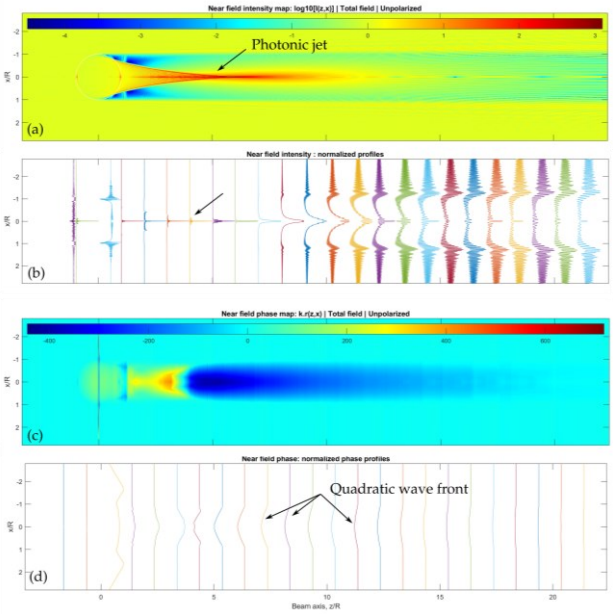

Figure 4 LMT: near-field of a methanol droplet in air with radius a≈101.6μm and m=1.3145 (λ=0.532μm, zc=0.1m). (a) Logarithm of the normalized electromagnetic intensity and (b) corresponding transverse profiles; corresponding (c) phase map and transverse profiles.

Even with the parallelization option, high-resolution holograms of large particles can take a long time to compute, especially if the particles are far away from the sensor. The latter limitation is due to the difficulty of accurately computing the Hankel functions at large distances from the particle. To reduce the computational effort, four solutions have been implemented. They allow the total computational time to be significantly reduced without noticeable loss of accuracy:

- For large distances, the Hankel function is computed using asymptotic expressions [59] instead of downward recurrence.

- Since the hologram of spherical particles is also rotationally symmetric, a special numerical scheme has been developed to interpolate the electromagnetic field components, over the entire sensor surface, from their values calculated along the CCD sensor diagonal.

- To account for the lateral shift of the particle coordinates $(x, y)_p$ with respect to the CCD coordinate system $(x, y)_c$, the electromagnetic calculations for each particle are performed only for the diagonal of the sensor surface.

- The three complex components of each electric field are interpolated using a bilinear interpolation method before the Poynting vector is used to calculate the local electromagnetic intensity.

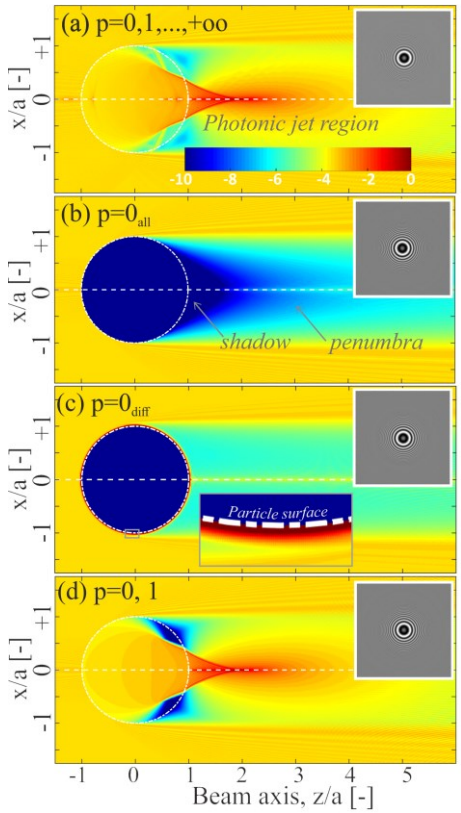

Figure 5 Debye expansion: logarithm of the normalized electromagnetic near-field intensity around a methanol droplet in air with radius a≈101.6μm and m=1.3145 (λ=0.532μm, z_c=0.1m): (a) all scattering processes included; (b) only p=0all term: specular reflection, surface waves and tunnelling contributions; (c) only pure diffraction; (d) only single refraction and p=0all terms.

3.3 Debye expansion and localized principle

For DIH operating in the small angle scattering regime, it is commonly assumed that holograms result exclusively from a pure diffraction process. This is an implicit assumption when, for example, the opaque disc model is used to model the wavefront exiting the particle [60]. In fact, this term, denoted here as p=0all, includes several contributions: the pure diffraction term (independent from the material properties and denoted here as p=0diff), which does not depend on the material properties of the particle (i.e. the refractive index) [61, 62]); specular reflection below and above the grazing incidence region, tunnelling and surface waves. As mentioned above, except for the term p=0diff, all other optical phenomena are generally neglected in the DIH literature - without any clear justification. Meanwhile, the PJM (see below) is a clear proof that it is mandatory to consider the term p=1 (single refraction) [1-3]. The results obtained with the Debye expansion, combined with the localisation principle, show that this term is not sufficient to reproduce all the fine structure of the PJ. To achieve this, it is necessary to consider the interference of the terms p=0all and p=1 on the DIH sensor, while the influence of higher refractive terms (p>1) is consistently less critical, as shown in Figure 5.

3.4 Asymptotic models for hologram formation

Following the previous remarks, the authors have developed an asymptotic model for the forward scattering of spherical particles. In this model, the contributions of pure diffraction, specular reflection and surface waves are described by an approximation, derived by Nussensweig [63], of the first two terms of the Debye expansion. These terms can be rewritten, using Fraunhofer or Rayleigh-Sommerfeld integrals, as a diffraction problem involving an opaque disc and a thin concentric ring with a complex outer radius. This complex boundary allows some of the effects associated with the refractive index of the particle to be taken into account in the forward scattering.

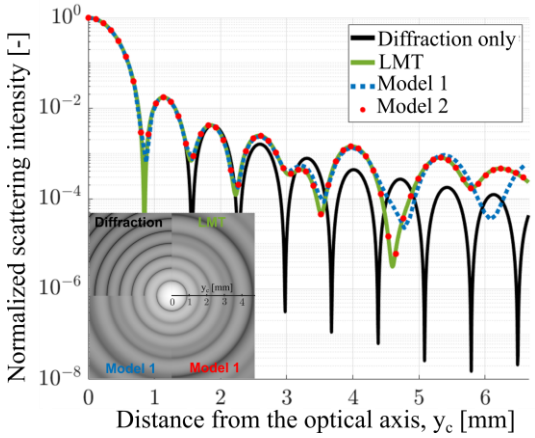

Figure 6 Scattering of a plane wave (λ=0.633μm) by a water droplet in air, with radius a=45μm, observed at a distance of z_c=10cm. Comparison of the logarithm of the normalised electromagnetic near-field intensity obtained with LMT and three models: pure diffraction, opaque disk and annular ring approximation with Fresnel integrals (Model 1) and Rayleigh-Sommerfeld integrals (Model 2). The thumbnail shows the corresponding holograms.

The other part, induced by the rays hitting the surface of the particle, is modelled with a Geometric Optics

Approximation (GOA) valid in the near and the far field. Figure 6 shows a typical result for a water drop observed at z_c=10 cm. An extensive numerical study has demonstrated the efficiency and accuracy of this model (Model 2) over a wide range of distances, particle sizes, and refractive indices. More details will be provided during this conference, with the work presented by Chabrol and Onofri [64].

4 Measurement of particle refractive index

4.1 Background

In various realms of research and industry, understanding the composition of particles holds significant importance. With DIH, there are three different approaches to this measurement. The first one relies on morphological assessments, which necessitate stringent geometric-compositional relationships to size and classify suspended particles [11]. The second involves direct comparisons, such as using a best-fitting technique, between experimental holograms and their numerical simulations utilizing rigorous electromagnetic light scattering theories such as LMT [65, 66]. However, the computational requirements associated with these comparisons may prove prohibitive, especially for large particles in the range of few tens to several thousand micrometres, as pertinent to our investigations on multiphase flows. The third approach is the Photonic jet method (PJM) [1-3].

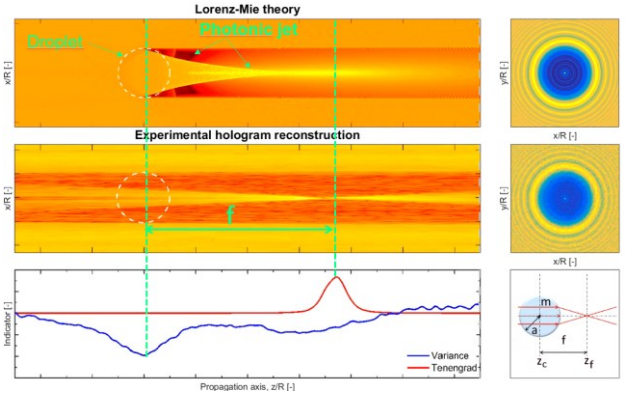

Figure 7 Principle of the photonic jet method in DIH: (a) direct calculation with LMT of the near-field of a droplet (a=0.55mm, m=1.0825) and (d) corresponding hologram (z_c=10cm, λ=0.475μm); (e) similar experimental hologram and (b) reconstructed near-field by the backpropagation of the experimental hologram; (c) evolution of the focusing indicators identifying the particle position and the focusing point.

4.2 Photonic jet method (PJM)

The PJM builds upon the concept that the forward contribution of the term p=1 of a large, transparent and spherical particle closely resembles that of the focusing of a ball lens with focal length, f. In the paraxial approximation, its focal length is contingent to its radius and real refractive index [60]:

$$f = ma/\left(2(m-1)\right) \quad (2)$$

Leveraging classical DIH back-propagation techniques enables the determination of the radius a and axial position of the particle. By localizing the focal point in (also referred as the maximum of the geometric caustic in physical optics [67] or 'photonic jet' (PJ) in electromagnetism [68]) of the ball lens, it can be directly estimated from the focal equation, Eq. (2). Tian et al. [4] were probably among the first to report the possibility to use this phenomenon to determine the refractive index of droplets and bubbles. Choi and Lee [12] have also utilized the ball lens analogy to refine the positioning of particles with known refractive indices. However, the present authors have independently advocated and demonstrated its capabilities for particle material recognition and estimate their refractive index.

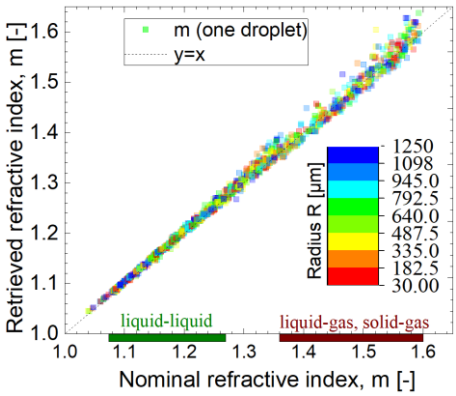

Figure 8 Numerical evaluation of the expected resolution of the PJM, using the ball lens equation, for a wide range of particle relative index and size ranges.

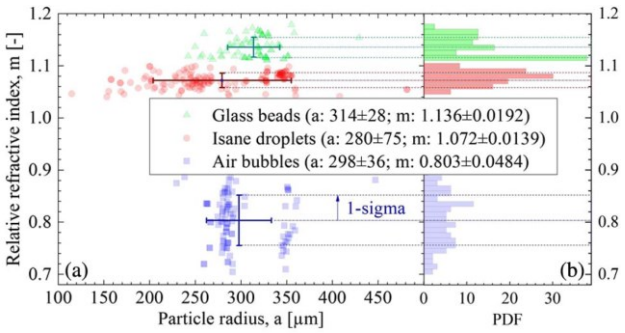

Figure 9 Experimental evaluation of the size and relative refractive index of air bubbles, Isane droplets and glass beads flowing in water.

Now referred as to the "photonic jet method" (PJM) in the DIH, it works well for both refractive particles (m>1, e.g. droplets and beads in gas or liquids) and reflective particles (m<1, gas bubbles in liquids or some liquid droplets in liquids). As shown in Figure 8, simulations show that the PJM allows to obtain, with almost no

additional computational cost, an accuracy of ±3.7 10^{-3} on the refractive index of liquid-liquid particles with radius in the range [30-1250] μm. This order of magnitude has been confirmed by experimental work on a four-phase flow, see Figure 9.

To further improve the performance and accuracy of the PJM, it is essential to develop a more sophisticated model for the so-called focal equation. This is precisely the aim of the work that is being carried out on asymptotic models of the forward scattering patterns, §3.3 and &3.4.

5 Reduction of the sensor filling rate

The maximum density of the particle field that can be characterised by DIH depends on many factors. These include DIH assumptions such as the absence of multiple scattering and an unperturbed incident wave, the resolution of direct or inverse restitution methods, the actual density of the particle cloud and the homogeneity of its spatial distribution, the observation distance, or the dynamic range of the sensor. There is little in the literature on this large and complex problem. However, the authors have recently investigated the possibility of using compression optics to reduce the fill rate ξ of the sensor by holograms. As an illustration of the method, Figure 10 compares the holograms recorded without and with compression optics for a stream of droplets. As a rough approximation, the gain of the method is of the order of $\left(a^2/\lambda z_c\right)^{-1}$, i.e. the inverse of the Fresnel number.

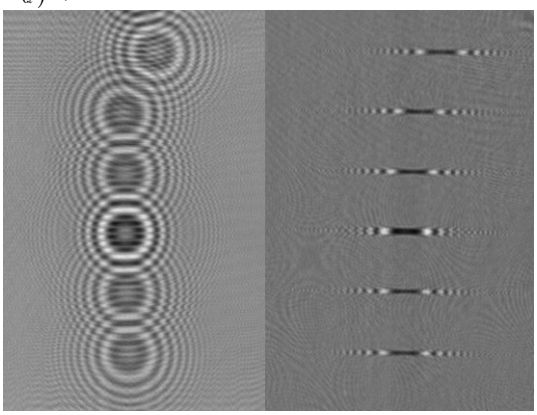

Figure 10 Experimental evidence of the ability of compression optics to reduce the sensor fill rate: left, free space; right, with compression optics. The droplets in these two experiments are similar but not identical.

6 Conclusion

After summarizing the basics of the DIH, the authors review their recent contributions to further enhance its capabilities, particularly in the asymptotic modelling and understanding of hologram formation, refractive index measurements, and sensor filling rate reduction.

This work was partially supported by the Nuclear Energy Division of CEA (program DISN/PAREC); the French government, grants managed by the Agence Nationale de la Recherche (reference ANR-23-CE51-0023, ANR-13-BS09-0008).

7 References

[1] Sentis, M.P.L., F.R.A. Onofri, and F. Lamadie, Photonic jet reconstruction for particle refractive index measurement by digital in-line holography. Optics Express, 2017. **25**(2): p. 867-873.

[2] Sentis, M.P.L., F.R.A. Onofri, and F. Lamadie, Bubbles, drops, and solid particles recognition from real or virtual photonic jets reconstructed by digital in-line holography. Optics Letters, 2018. **43**(12): p. 2945-2948.

[3] Sentis, M.P.L., et al., Digital in-line holography for the characterization of flowing particles in astigmatic optical systems. Optics and Lasers in Engineering, 2017. **88**: p. 184-196.

[4] Tian, L., et al., Quantitative measurement of size and three-dimensional position of fast-moving bubbles in air-water mixture flows using digital holography. Applied Optics, 2010. **49**(9): p. 1549-1554.

[5] Pan, G. and H. Meng, Digital holography of particle fields: reconstruction by use of complex amplitude. Applied Optics, 2003. **42**(5): p. 827-833.

[6] Jüptner W., Digital Holography: Digital Hologram Recording, Numerical Reconstruction, and Related Techniques. 2010, Berlin: Springer.

[7] Dubois, F., et al., Focus plane detection criteria in digital holography microscopy by amplitude analysis. Optics Express, 2006. **14**(13): p. 5895-5908.

[8] Berg, M.J., Tutorial: Aerosol characterization with digital in-line holography. Journal of Aerosol Science, 2022. **165**: p. 106023.

[9] Picart, P. and J. Leval, General theoretical formulation of image formation in digital Fresnel holography. Journal of the Optical Society of America A, 2008. **25**(7): p. 1744-1761.

[10] Memmolo, P., et al., Refocusing criterion via sparsity measurements in digital holography. Optics Letters, 2014. **39**(16): p. 4719-4722.

[11] Davies, E.J., et al., Evaluating unsupervised methods to size and classify suspended particles using digital in-line holography. Journal of Atmospheric and Oceanic Technology, 2015. **32**(6): p. 1241-1256.

[12] Choi, Y.-S. and S.-J. Lee, High-accuracy three-dimensional position measurement of tens of micrometers size transparent microspheres using digital in-line holographic microscopy. Optics Letters, 2011. **36**(21): p. 4167-4169.

[13] Hinsch, K.D. and S.F. Herrmann, Holographic Particle Image Velocimetry. Measurement Science and Technology, 2004. **15**(4).

[14] Soulez, F., et al., Inverse problem approach in particle digital holography: out-of-field particle detection made possible. Journal of the Optical Society of America A, 2007. **24**(12): p. 3708-3716.

[15] Gire, J., et al., Digital holography of particles: benefits of the 'inverse problem' approach. Measurement Science and Technology, 2008. **19**(7): p. 074005.

[16] Shao, S., K. Mallery, and J. Hong, Machine learning holography for measuring 3D particle distribution. Chemical Engineering Science, 2020: p. 115830.

[17] Barber, S.C. and P.W. Hill, Light Scattering by particles : computational methods. 1990, London: World Scientific.

[18] Hovenac, E.A. and J.A. Lock, Assessing the contribution of surface waves and complex rays to far-field scattering by use of the Debye series. J. Opt. Soc. Am. A, 1992. **9**(5): p. 781-795.

[19] Lugovtsov, A.E., A.V. Priezzhev, and S.Y. Nikitin, Light scattering by arbitrarily oriented optically soft spheroidal particles: Calculation in geometric optics approximation. Journal of Quantitative Spectroscopy and Radiative Transfer, 2007. **106**(1–3): p. 285-296.

[20] Fymat, A.L. and K.D. Mease, Mie forward scattering: improved semiempirical approximation with application to particle size distribution inversion. Applied Optics, 1981. **20**(2): p. 194-198.

[21] Ravey, J.C. and P. Mazeron, Light scattering by large spheroids in the Physical Optics Approximation: numerical comparison with other approximate and exact results. Journal of Optics, 1983. **14**(1): p. 29.

[22] Mishchenko, M.I., Far-field approximation in electromagnetic scattering. Journal of Quantitative Spectroscopy and Radiative Transfer, 2006. **100**(1): p. 268-276.

[23] Xu, F., K.F. Ren, and X. Cai, Extension of geometrical-optics approximation to on-axis Gaussian beam scattering. I. By a spherical particle. Applied Optics, 2006. **45**(20): p. 4990-4999.

[24] Onofri, F.R.A., et al., Physical-optics approximation of near-critical-angle scattering by spheroidal bubbles. Optics Letters, 2012. **37**(22): p. 4780-4782.

[25] Yu, H., F. Xu, and C. Tropea, Optical caustics associated with the primary rainbow of oblate droplets: simulation and application in non-sphericity measurement. Optics Express, 2013. **21**(22): p. 25761-25771.

[26] Duan, Q., et al., Generalized rainbow patterns of oblate drops simulated by a ray model in three dimensions. Optics Letters, 2021. **46**(18): p. 4585-4588.

[27] Duan, Q., et al., Numerical implementation of three-dimensional vectorial complex ray model and application to rainbow scattering of spheroidal drops. Optics Express, 2023. **31**(21): p. 34980-35002.

[28] Cheong, F.C., B.J. Krishnatreya, and D.G. Grier, Strategies for three-dimensional particle tracking with holographic video microscopy. Optics Express, 2010. **18**(13): p. 13563-13573.

[29] Zhang, Y. and X. Zhang, Reconstruction of a complex object from two in-line holograms. Optics Express, 2003. **11**(6): p. 572-578.

[30] Méès, L., et al., Evaporating droplet hologram simulation for digital in-line holography setup with divergent beam. Journal of the Optical Society of America A, 2013. **30**(10): p. 2021-2028.

[31] Yevick, A., M. Hannel, and D.G. Grier, Machine-learning approach to holographic particle characterization. Optics Express, 2014. **22**(22): p. 26884-26890.

[32] Lamadie, F., L. Bruel, and M. Himbert, Digital holographic measurement of liquid–liquid two-phase flows. Optics and Lasers in Engineering, 2012. **50**(12): p. 1716-1725.

[33] Marston, P.L., Critical angle scattering by a bubble: physical-optics approximation and observations. Journal of the Optical Society of America, 1979. **69**(9): p. 1205-1211.

[34] Onofri, F., M. Krysiek, and J. Mroczka, Critical angle refractometry and sizing of bubble clouds. Optics Letters, 2007. **32**(14): p. 2070-2072.

[35] Onofri, F.A., et al., Optical characterization of bubbly flows with a near-critical-angle scattering technique. Exp. in Fluids, 2009. **47**(4-5): p. 721-732.

[36] Saengkaew, S., et al., Rainbow refractrometry: On the validity domain of Airy's and Nussenzveig's theories. Opt. Commun., 2006. **259**(1): p. 7-13.

[37] Li, H., et al., The effect of initial diameter on rainbow positions and temperature distributions of burning single-component n-Alkane droplets. Journal of Quantitative Spectroscopy and Radiative Transfer, 2017. **195**: p. 164-175.

[38] Ouattara, M., et al., Droplet sizing and mixture fraction measurement in liquid flows with rainbow-angle diffractometry. Applied Optics, 2017. **56**(29): p. 8109-8120.

[39] Wu, X., et al., Self-calibrated global rainbow refractometry: a dual-wavelength approach. Chinese Optics Letters, 2017. **15**(4): p. 042902.

[40] van Beeck, J.P.A.J., T. Grosges, and M.G. De Giorgi, Global rainbow thermometry assessed by Airy and Lorenz-Mie theories and compared with phase Doppler anemometry. Applied optics, 2003. **42**(19): p. 4016-4022.

[41] Fabrice, L., M. Loïc, and F. Corinne, Holographie numérique en ligne appliquée aux mesures en mécanique des fluides. Techniques de l'ingénieur Mesures physiques, 2022. base documentaire : TIP672WEB(ref. article : r2163).

[42] Lebrun D., Belaïd S., and Özkul C., Hologram Reconstruction by use of Optical Wavelet Transform. Appl. Opt., 1999. **38**(17): p. 3730-3734.

[43] Zhang, W., et al., Twin-Image-Free Holography: A Compressive Sensing Approach. Physical Review Letters, 2018. **121**(9): p. 093902.

[44] Denis, L., et al., Numerical suppression of the twin image in in-line holography of a volume of micro-objects. Measurement Science and Technology, 2008. **19**(7): p. 074004.

[45] Latychevskaia, T. and H.-W. Fink, Solution to the Twin Image Problem in Holography. Physical Review Letters, 2007. **98**(23): p. 233901.

[46] Lee, S.-H., et al., Characterizing and tracking single colloidal particles with video holographic microscopy. Optics Express, 2007. **15**(26): p. 18275-18282.

[47] Berdeu, A., et al., Reconstruction of in-line holograms: combining model-based and regularized inversion. Optics Express, 2019. **27**(10): p. 14951-14968.

[48] Jolivet, F., et al., Regularized reconstruction of absorbing and phase objects from a single in-line hologram, application to fluid mechanics and micro-biology. Optics Express, 2018. **26**(7): p. 8923-8940.

[49] Mallery, K. and J. Hong, Regularized inverse holographic volume reconstruction for 3D particle tracking. Optics Express, 2019. **27**(13): p. 18069-18084.

[50] Walcutt, N.L., et al., Assessment of holographic microscopy for quantifying marine particle size and concentration. Limnology and Oceanography: Methods, 2020. **18**(9): p. 516-530.

[51] Kim, M.K., Principles and techniques of digital holographic microscopy. SPIE Reviews, 2010. **1**(1): p. 1-51, 51.

[52] Kemper, B. and G. von Bally, Digital holographic microscopy for live cell applications and technical inspection. Applied Optics, 2008. **47**(4): p. A52-A61.

[53] Garcia-Sucerquia, J., et al., Digital in-line holographic microscopy. Applied Optics, 2006. **45**(5): p. 836-850.

[54] Ferraro, P., et al., Extended focused image in microscopy by digital holography. Optics Express, 2005. **13**(18): p. 6738-6749.

[55] Latychevskaia, T., Iterative phase retrieval for digital holography: tutorial. Journal of the Optical Society of America A, 2019. **36**(12): p. D31-D40.

[56] Bohren, C.F. and D.R. Huffman, Absorption and scattering of light by small particles. 1998, New york: Wiley & Sons.

[57] Onofri, F., G. Gréhan, and G. Gouesbet, Electromagnetic scattering from a multilayered sphere located in an arbitrary beam. Applied optics, 1995. **34**(30): p. 7113-7124.

[58] Wiscombe, W.J., Improved Mie scattering algorithms. Applied Optics, 1980. **19**(9): p. 1505-1509.

[59] Abramowitz, M. and I.A. Stegun, Handbook of mathematical Functions. 1965, New-York: Dover inc.

[60] Goodman, J.W., Introduction to Fourier Optic. Mac. Graw-Hill, New York, 1960.

[61] Lock, J.A. and P. Laven, Mie scattering in the time domain. Part II. The role of diffraction. Journal of the Optical Society of America A, 2011. **28**(6): p. 1096-1106.

[62] Nussenzveig, H.M., Diffraction effects in semiclassical scattering. 1992, Cambridge: Cambridge University Press.

[63] Nussenzveig, H.M., High-Frequency Scattering by a Transparent Sphere. I. Direct Reflection and Transmission. Journal of Mathematical Physics, 1969. **10**(1): p. 82-124.

[64] Chabrol, L. and F.R.A. Onofri. Refractring and Diffracting Ring Effects In Digital In-Line Holography. in 14th international conference series on Laser-light and Interactions with Particles (LIP). 2024. Xi'an, Shaanxi, China.: Xidian University.

[65] Shpaisman, H., B.J. Krishnatreya, and D.G. Grier, Holographic microrefractometer. Applied Physics Letters, 2012. **101**(9): p. 091102.

[66] Reconstruction of refractive-index distribution in off-axis digital holography optical diffraction tomographic system. Opt. Express, 2009. **17**: p. 13758.

[67] Nye, J.F., Natural Focusing and Fine Structure of Light: Caustics and Wave Dislocations. 1999, London: IOP Publishing Ltd.

[68] Lecler, S., Y. Takakura, and P. Meyrueis, Properties of a three-dimensional photonic jet. Optics Letters, 2005. **30**(19): p. 2641-2643.